

Biofabrication



PAPER

Expanding sacrificially printed microfluidic channel-embedded paper devices for construction of volumetric tissue models *in vitro*

RECEIVED

16 March 2020

REVISED

31 July 2020

ACCEPTED FOR PUBLICATION

20 August 2020

PUBLISHED

17 September 2020

Hongbin Li^{1,2,3,7}, Feng Cheng^{1,3,7}, Wanlu Li¹, Xia Cao¹, Zixuan Wang¹, Mian Wang¹, Juan Antonio Robledo-Lara^{1,4}, Junlong Liao¹, Carolina Chávez-Madero^{1,5}, Shabir Hassan¹, Jingwei Xie⁶, Grissel Trujillo-de Santiago⁵, Mario Moisés Álvarez⁵, Jinmei He³ and Yu Shrike Zhang^{1,8} 

¹ Division of Engineering in Medicine, Brigham and Women's Hospital, Department of Medicine, Harvard Medical School, Cambridge, MA 02139, United States of America

² College of Light Industry and Textile, Qiqihar University, Qiqihar, Heilongjiang 161000, People's Republic of China

³ MIT Key Laboratory of Critical Materials Technology for New Energy Conversion and Storage, School of Chemistry and Chemical Engineering, Harbin Institute of Technology, Harbin, Heilongjiang 150001, People's Republic of China

⁴ Departamento de Ingeniería Mecatrónica y Eléctrica, Escuela de Ingeniería y Ciencias, Tecnológico de Monterrey, CP78211, San Luis Potosí, San Luis Potosí, Mexico

⁵ Centro de Biotecnología-FEMSA, Tecnológico de Monterrey, Monterrey CP 64849, Mexico

⁶ Holland Regenerative Medicine Program, University of Nebraska Medical Center, Omaha, NE 68198, United States of America

E-mail: yszhang@research.bwh.harvard.edu

Keywords: bacterial cellulose, 3D printing, microfluidics, paper-based tissue model, tissue engineering, tissue model engineering
Supplementary material for this article is available [online](#)

Abstract

We report a method for expanding microchannel-embedded paper devices using a precisely controlled gas-foaming technique for the generation of volumetric tissue models *in vitro*. We successfully fabricated hollow, perfusable microchannel patterns contained in a densely entangled network of bacterial cellulose nanofibrils using matrix-assisted sacrificial three-dimensional printing, and demonstrated the maintenance of their structural integrity after gas-foaming-enabled expansion in an aqueous solution of NaBH₄. The resulting expanded microchannel-embedded paper devices showed multilayered laminar structures with controllable thicknesses as a function of both NaBH₄ concentration and expansion time. With expansion, the thickness and porosity of the bacterial cellulose network were significantly increased. As such, cellular infiltration was promoted comparing to as-prepared, non-expanded devices. This simple technique enables the generation of truly volumetric, cost-effective human-based tissue models, such as vascularized tumor models, for potential applications in preclinical drug screening and personalized therapeutic selection.

1. Introduction

Three-dimensional (3D) printing has emerged as a powerful enabler in medical and biomedical applications [1, 2]. The technology allows the generation of structurally relevant scaffolds to support the attachment, growth, migration, and functioning of cells through its ability to pattern biomaterials in an automated and spatially defined manner [3, 4]. To date, numerous biocompatible/bioactive materials have been adopted and optimized for 3D printing, including plastic polymers such as poly(lactic-co-glycolic) acid [5], polycaprolactone [6], poly(glycerol

sebacate) [7], hydrogels such as gelatin methacryloyl [8, 9], poly(ethylene glycol) [10], and alginate [11], or their combinations [12–15].

These various 3D printing strategies have significantly enhanced our capacity to undertake challenging problems in biomedicine [16, 17]. In particular, the development of microphysiological systems is currently the focus of interest of numerous research efforts. Microphysiological systems, or organ-on-a-chip systems, are microfluidic platforms hosting biomimetic microscale human tissue or organ units. Microphysiological systems are typically configured in a volumetric manner, which along with the dynamic physicochemical cues provided by the microfluidic device, would enable the faithful and functional reproduction of their native counterparts

⁷ These authors contributed equally to this work.

⁸ Author to whom any correspondence should be addressed.

outside the human body [18, 19]. As such, micro-physiological systems could facilitate improved accuracy and precision in screening the responses of human tissues and organs toward drugs [20], chemicals [21], biomaterials [22], nanoparticles [23], or biological species [24] in comparison to the conventional planar, static dish-based cell cultures [25]. They are also expected to surpass the performance of pre-clinical animal models in selected scenarios such as disease modeling that may not be readily recapitulated in animals [26]. The interconnection of multiple organ-on-a-chip devices will further allow emulating the compartmentalization of the human body and will enable recapitulation of pharmacodynamics and pharmacokinetics, such as simultaneous studies on anti-cancer drug efficacy and toxic side effects [27, 28]. To date, most human tissues and organs have been modeled in chip-based devices, ranging from the brain [29] and the nervous system [30] to the heart [31], lung [32], eye [33], gastrointestinal system [34], liver [35], kidney [36], skeletal muscle [37], bone [38], cartilage [39], and to various disorders such as cancer [40] and neurodegenerative diseases [41].

Despite all these successes, current organ-on-a-chip platforms are still limited by a few application-dependent drawbacks: (i) relatively complicated microfabrication procedures and expensive capital equipment needed for generating the microfluidic chip devices; and (ii) the short shelf-lives associated with the tissue/organ models requiring their immediate usage post-fabrication (i.e. when hydrogels are used, such as when combined with 3D bioprinting). For the latter, bacterial cellulose has been demonstrated to be an interesting functional biomaterial among a variety of natural polymers [42, 43]. Bacterial cellulose is extracellularly synthesized by the bacterium *Acetobacter xylinum* (*A. xylinum* X-2), which possess distinct features including good mechanical strength, high crystallinity, ultrafine nanofibrils forming networked bulk structures [44–46], high water-holding capacity [47], and excellent biocompatibility [48].

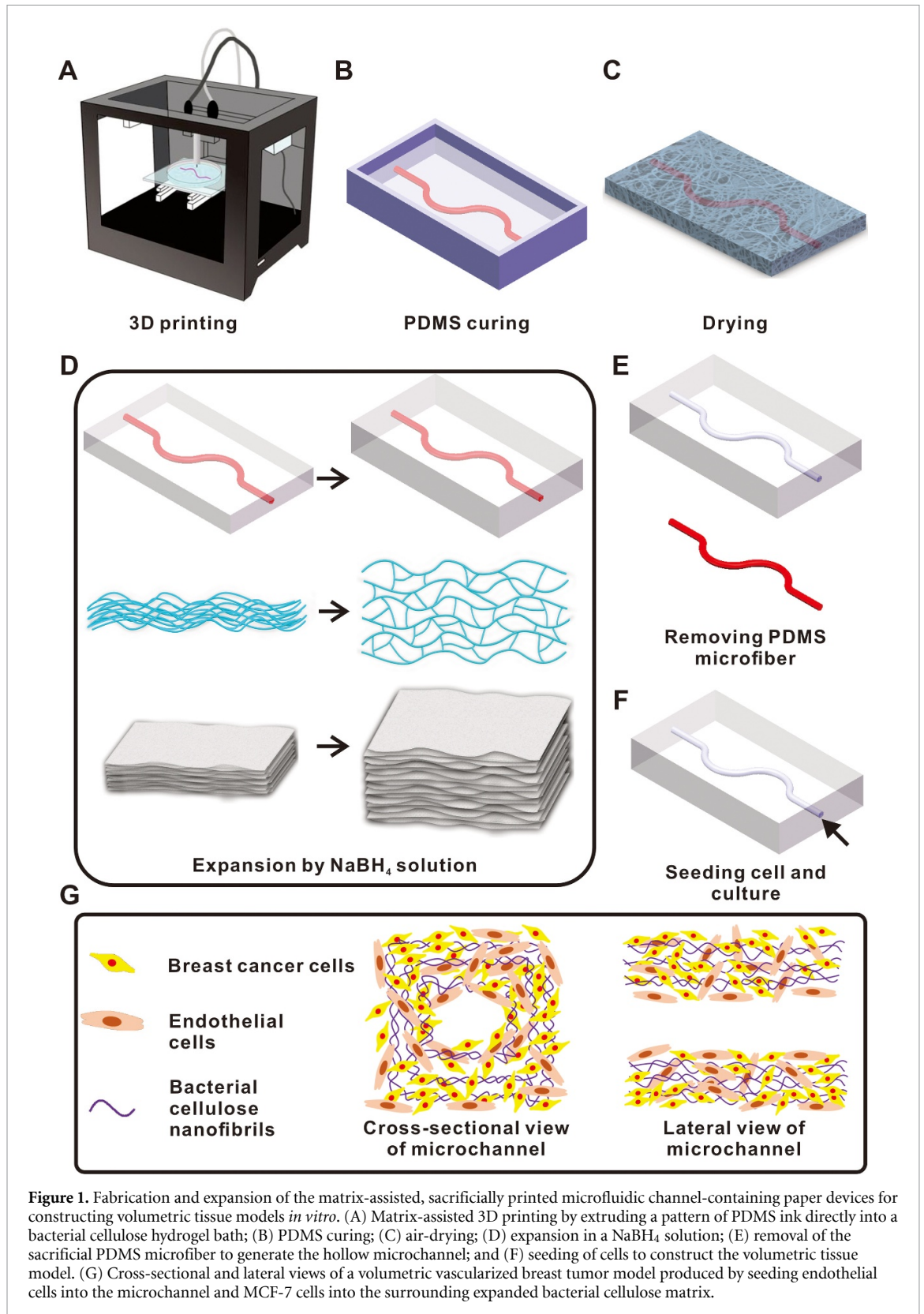
Bacterial cellulose has been widely adopted as a scaffolding biomaterial in the engineering of biomimetic tissues and their models, showing appropriate cellular responses and behaviors [49–51]. In fact, in a previous study, we successfully demonstrated the fabrication of well-defined microfluidic channel structures embedded in a bacterial cellulose hydrogel using a matrix-assisted 3D printing method [52]. Upon drying, the embedded sacrificial ink could maintain its integrity and be subsequently removed, forming paper-based microfluidic chip devices containing sophisticated microchannel networks that are typically hard to produce using conventional fabrication strategies [53, 54]. Moreover, due to the low cost of the materials used (i.e. bacterial cellulose and the sacrificial ink), as well as the automated 3D

printing process employed, we were able to lower the cost of fabrication of the devices to only a few cents per piece. Furthermore, our low-cost, microchannel-embedded paper-based microfluidic devices could then be rehydrated and seeded with desired cell types in different compartments to construct physiologically relevant tissue models such as a vascularized breast tumor model.

While this new strategy has significantly elevated our ability to produce cost-effective organ-on-a-chip systems, a critical disadvantage lies in the fact that the nanofibrils of bacterial cellulose would inevitably form a dense mesh during the initial dehydration process, thus restricting cell infiltration as we previously observed [52]. This is consistent with the literature, which has indicated that bacterial cellulose usually generates uncontrollable and packed networks [55], leading to tightly entangled, two-dimensional (2D)-like nanofibril mats/membranes resistant to both cell infiltration and growth within the scaffold volumes [56–58].

Several attempts have been made to produce 3D bacterial cellulose nanofibril scaffolds more capable of inducing cell ingrowth. For example, the combination of acetic acid treatment and freeze-drying to enhance the porosity profile of bacterial cellulose scaffolds has been proposed [59]. Others prepared microporous bacterial cellulose scaffolds by adding 300 to 500 μm paraffin wax microspheres or starch particles during fermentation; after producing bacterial cellulose, the particles were removed to enable formation of larger pores [50]. Studies regarding endothelial cells, smooth muscle cells, and chondrocytes indicated that these cells would adhere to bacterial cellulose, showing good biocompatibility [46, 50, 60]. Bacterial cellulose scaffolds with micropores have been also fabricated by a repeated freeze-drying method. These matrices were used in the culture of cancer cells, which were observed to spread in the scaffolds showing no negative effects on cell viability and proliferation [61, 62].

While effective overall, the abovementioned methods of pore formation are either time-consuming, uncontrollable, or incompatible with 3D printing. A fast, controllable, and effective way to generate truly 3D bacterial cellulose nanofibril scaffolds to combine with our matrix-assisted sacrificial printing for improved *in vitro* tissue modeling is consequently, in urgent demand. To this end, an efficient gas-foaming method for expanding electrospun polymer nanofiber mats to 3D scaffolds with well-controlled thicknesses as well as porosities was previously developed [56, 63, 64]. Here, we seek to demonstrate the feasibility of adopting and optimizing such gas-forming strategy for the expansion of our sacrificially printed microfluidic channel-embedded paper chip devices and their use in constructing volumetric tissue models *in vitro* (figure 1). Specifically, we used a silicone elastomer-based sacrificial ink to be



deposited within a bacterial cellulose hydrogel matrix (figure 1(A)), which could be subsequently air-dried to form a paper-like membrane (figures 1(B) and (C)), very much similar to that obtained using our original method [52]. Unlike the semi-solid petroleum jelly-liquid paraffin ink utilized before, the solid silicone elastomer-based ink, when cured, was

shown to resist the expansion process, a treatment by immersing the membrane in a sodium borohydride (NaBH_4) aqueous solution, and maintain the integrity of its cylindrical microfibrillar shape (figure 1(D)). Afterwards, the hollow perfusable microfluidic channel could be formed by extracting the silicone elastomer sacrificial microfiber (figure 1(E)).

Finally, relevant cells could be introduced into the microchannel and the surrounding expanded, multi-layer bacterial cellulose matrix to enable construction of a truly volumetric tissue model for drug screening (figures 1(F) and (G)).

2. Materials and methods

2.1. Materials

Bacterial cellulose membranes were purchased from Hainan Yide Industry Co. Ltd. (China). Sylgard 184 and SE 1700 were purchased from Dow Corning (USA). NaBH_4 analytical grade was purchased from Sigma-Aldrich (USA). Phosphate-buffer saline (PBS, ThermoFisher, USA) and other solutions were prepared with deionized water (18.2 M Ω cm, Millipore, USA).

2.2. Production of the bacterial cellulose hydrogel bath

0.4–1.0 w/v% bacterial cellulose hydrogels were obtained by washing using an 8 w/v% alkaline (NaOH, Sigma-Aldrich) solution and subsequently mechanical pulping (Hamilton Beach, USA) at a high agitation speed of 10 000 rpm [52, 65].

2.3. Ink preparation

The polydimethylsiloxane (PDMS) inks were formulated by blending two PDMS materials, Sylgard 184 and SE 1700 [66]. Both Sylgard 184 and SE 1700 base materials were first blended with their respective curing agents at a 10:1 (base:curing agent) ratio by mass. They were then separately placed for 15 min in a vacuum desiccator for degassing. The PDMS inks were subsequently prepared by mixing Sylgard 184 and SE 1700 at five different mass ratios (10:0, 7:3, 5:5, 3:7, and 0:10). Finally, the inks were loaded into a 10 ml syringe (Becton Dickinson, USA) at room temperature and centrifuged for 5 min at 5000 rpm in a Sorvall Legend X1R Centrifuge (ThermoFisher, USA) to eliminate air bubbles.

2.4. Rheological measurements of the bacterial cellulose hydrogel baths and the inks

Characterizations of the rheological properties of the bacterial cellulose hydrogel and the PDMS inks with different compositions were performed by using a hybrid rheometer (HR-3, Waters, USA). The bacterial cellulose matrix was constantly shaken (3200 rpm) at room temperature before the tests to prevent sedimentation, while the PDMS inks were vigorously stirred at room temperature before keeping them stationary to remove bubbles. Under a shear ramp mode running from 0.01 to 1000 s^{-1} with a 1000 μm gap size at 25 °C (the temperature for printing), their rheological behaviors were assessed. In addition, an oscillation amplitude sweep was carried out to measure the storage moduli (G') and the loss moduli

(G'') of the bacterial cellulose suspensions at a constant strain of 0.1%, which was within the linear viscoelastic region, and over a frequency range from 0.1 to 100 Hz.

2.5. Printability analysis

The 3D microfibrinous patterns were fabricated by directly extruding the Sylgard 184/SE 1700 blend ink into baths of bacterial cellulose hydrogels using a bioprinter (Allevi I, Allevi Inc. USA). The 3D patterns were first created using SolidWorks (Dassault Systèmes, France) and the G-code was generated with the support of the bioprinter slicing software (Repetier-Host V1.6.1, Hot-World GmbH & Co. KG, Germany). The PDMS ink was loaded into a 10 ml syringe at room temperature, which was then tipped with a 23G needle as the nozzle. The extrusion pressure was regulated by the pressure control unit equipped with a built-in air pump. Printability was analyzed for the four different ink compositions (Sylgard 184:SE 1700 at 7:3, 5:5, 3:7, and 0:10), four different bacterial cellulose concentrations (0.4, 0.6, 0.8, and 1.0 w/v%), four different printing speeds (6, 8, 10, and 12 mm s^{-1}), and four different extrusion pressures (70, 75, 80, and 85 kPa).

2.6. Preparation of microchannel-embedded paper devices

The paper devices containing embedded microchannels were obtained by removing the cured PDMS microfibrils at room temperature. After matrix-assisted printing, the pattern of the PDMS ink in a bacterial cellulose matrix was cured in an oven at 80 °C for 2 h in a closed container to avoid water evaporation during curing. To form a paper-like membrane, the entire matrix was subsequently air-dried at room temperature for 48 h.

2.7. Expansion of microchannel-embedded paper devices

NaBH_4 aqueous solutions were used to expand the microchannel-containing paper devices, as they have been extensively investigated for H_2 generation due to its controllable hydrolysis reaction and relatively high hydrogen content (10.8%) [67]. The devices were immersed in 50 ml of deionized water or freshly prepared NaBH_4 solutions at 0.01, 0.1, and 1 M, and gently shaken at 50 rpm for different time periods (5, 10, 20, 30, and 45 min). The expanded specimens were then rinsed three times with deionized water after removing the NaBH_4 solutions. Next, a mild vacuum was applied to eliminate trapped gas bubbles within the microchannel-embedded paper devices. Finally, the PDMS elastomeric microfibrils were carefully extracted from the surrounding matrices after freeze-drying, to obtain hollow, perfusable microchannels.

2.8. Characterizations of the expanded microchannel-embedded paper devices

The thicknesses of the expanded microchannel-embedded paper devices and the diameters of the microchannels were measured using a digital caliper. To obtain their cross-sections, the samples were freeze-dried and gently cut. Before and after expansion, the surfaces and cross-sections of the microchannel-embedded paper devices were visualized using scanning electron microscopy (SEM, Zeiss, Germany). SEM images were acquired at an accelerating voltage of 30 kV s⁻¹ following sputter-coating the specimens with gold.

The porosities of the expanded microchannel-embedded paper devices were calculated according to the volume changes pre- and post-expansion. Porosity was derived according to the following equation:

$$\varepsilon = \frac{V - V_0}{V} \times 100\%,$$

where ε is porosity, $V = L$ (length) \times W (width) \times T (thickness) is the volume of the expanded microchannel-embedded paper device, $V_0 = \frac{m_0}{\rho_0}$ is the calculated volume of bacterial cellulose, m_0 is the mass of bacterial cellulose, and ρ_0 is the density of bacterial cellulose.

The capillary effect of the microchannel-embedded paper devices with different expansion times was also assessed. For better visualization of the capillary effect, fluorescent microbeads of desired colors at 0.1 v/v% were used.

The compressive properties of the microchannel-embedded paper devices were performed by using a mechanical tester (Instron 3342, USA) at a strain rate of 5 mm min⁻¹ under room temperature.

2.9. Cell culture

In our study, three different cell types were used to fulfill the experimental requirements, human umbilical vein endothelial cells (HUVECs; green fluorescent protein (GFP)-tagged or unlabeled; Angio-Proteomie, USA), MCF-7 breast tumor cells (ATCC, USA), and MDA-MB-231 breast cancer cells (HTB-26, ATCC). Endothelial growth medium (EGM, Lonza) supplemented with 1 v/v% antibiotic-antimycotic (ThermoFisher), was used to culture the HUVECs. Dulbecco's modified Eagle's medium (ThermoFisher) supplemented with 10 v/v% fetal bovine serum (ThermoFisher) and 1 v/v% antibiotic-antimycotic was used to culture MCF-7 cells or MDA-MB-231 cells. The cells were cultivated at 37 °C and 5 v/v% CO₂ until 70% confluency. Prior to cell seeding, the expanded microchannel-embedded paper devices were autoclaved for 15 min to sterilize with simultaneous hydration. Subsequently, fibronectin (50 ng ml⁻¹) was injected into the microchannels and incubated at 4 °C for 12 h for coating. HUVECs were seeded into the microchannels at a density of 1 \times 10⁷

cells ml⁻¹ for 1 h, and the constructs were flipped for another hour to ensure uniform cell attachment on the microchannel surfaces. In the case of co-culture, after 12 h of HUVECs seeding, MCF-7 cells (2 \times 10⁶ cells ml⁻¹) were further inoculated into the matrices of the paper devices and cultured in EGM.

2.10. Cell viability and morphology analyses

The cell viability was evaluated by staining using a Live/Dead[®] Cell Viability Kit (ThermoFisher) according to the manufacturer's instructions at days 1, 3, 7, and 14 after cell seeding in the expanded, microchannel-embedded paper devices. The samples were stained using phalloidin/4',6-diamidino-2-phenylindole (DAPI) for F-actin/nuclei, followed by observation under an inverted fluorescence microscope (Nikon Ti-E, Japan) or a Zeiss Confocal Fluorescence Microscope (LSM880 with Airyscan). Mouse-anti human CD31 primary antibody (Abcam, USA) was diluted at 1:200 in PBS containing 5 v/v% goat serum (ThermoFisher) and 0.2 v/v% Triton X-100 (Sigma-Aldrich) for overnight at 4 °C. After washing three times with PBS, the samples were further incubated with Alexa Fluor 594-goat anti-mouse secondary antibody (1:200, ThermoFisher) at 4 °C for overnight. Cell Tracker[™] Red CMTPX Dye (ThermoFisher) was used to mark the MCF-7 cells when necessary. At least six images from different areas were randomly selected to calculate the number of live and dead cells using ImageJ (National Institutes of Health, USA), and the cell viability was expressed as the percentage of the number of live cells to the total cell number.

2.11. Cisplatin treatment

For cisplatin treatment, 0, 125, or 250 μ M of cisplatin was infused into the microchannels after 24 h of culture of the vascularized breast tumor models in the expanded paper devices, and the samples were cultured for another 48 h. Cell viability was subsequently calculated as described above.

2.12. Statistical analysis

All data were presented as means \pm standard deviations of at least three independent experiments with each experiment including at least triplicates. Student's t-test was used for comparison among various experimental and control groups. P-values of less than 0.05 were considered statistically significant.

3. Results and discussions

3.1. Rheological evaluations of the inks and the bacterial cellulose hydrogel baths

During matrix-assisted 3D sacrificial printing as the nozzle moves inside the bacterial cellulose bath, the PDMS ink was extruded and deposited into a microfibrillar pattern with a defined shape. We first investigated the rheological behaviors of PDMS inks,

formed by blending Sylgard 184 with SE 1700 at various mass ratios to achieve suitable strengths for printing at room temperature. As revealed in figure 2(A), the viscosity of the PDMS ink increased with the decreasing Sylgard 184:SE 1700 ratio from 10:0 to 0:10. Results indicated that the PDMS inks that contained a higher Sylgard 184 concentration became less viscous. Moreover, all the inks made of Sylgard 184:SE 1700 ratios at 0:10, 3:7, 5:5, and 7:3 possessed shear-thinning behaviors. Interestingly, the PDMS ink made of entirely Sylgard 184 (i.e. 10:0 of Sylgard 184:SE 1700) showed a poor shear-thinning characteristic in the frequency range evaluated.

Similarly, the rheological behaviors of the bacterial cellulose suspensions also played a critical role in determining printability. We used four different concentrations (0.4, 0.6, 0.8, and 1.0 w/v%) of bacterial cellulose suspensions and measured their viscosities. Within the shear rate range evaluated, all groups had an approximate linear logarithmic relationship between the viscosity and the shear rate. As expected, the viscosity increased as a function of bacterial cellulose concentration (figure 2(B)). Likewise, the sol-gel transition and creep recovery from the stresses exerted on the bacterial cellulose suspensions with different concentrations were also investigated by oscillatory rheological measurements. The moduli of bacterial cellulose suspensions increased when the bacterial cellulose concentration was increased (figure S1 (available online at stacks.iop.org/BF/12/045027/mmedia)). The storage moduli (G') were larger than the loss moduli (G'') at all frequencies analyzed, indicating that the bacterial cellulose suspensions were behaving like a non-flowing solid. Such observation suggested that bacterial cellulose suspensions might have potential applications as gelling, stabilizing, and emulsifying agents, or more relevant to the current work, as support materials [68, 69].

3.2. Printability assessments

The printability of the various formulations of PDMS inks and bacterial cellulose baths was subsequently assessed, based on the structural integrity of the printed ink microfibers inside the baths, before and after drying of the bacterial cellulose hydrogels. When SE 1700 was dominant in the ink compositions, the printed lines were always incomplete likely due to the overly high viscosities of the inks (figure 2(C)–(E)). When the ink was purely made of SE 1700, the viscosity was too high to be extruded using our 3D printing platform (unattainable pressure range), and thus this formulation was not further studied for printability. Instead, the PDMS inks with high Sylgard 184 concentrations did not form continuous printed lines in the bacterial cellulose hydrogel baths. This was mainly attributable to the relatively high fluidity of Sylgard 184 that could not hold the shapes of the extruded ink microfibers. Further considering the interactions

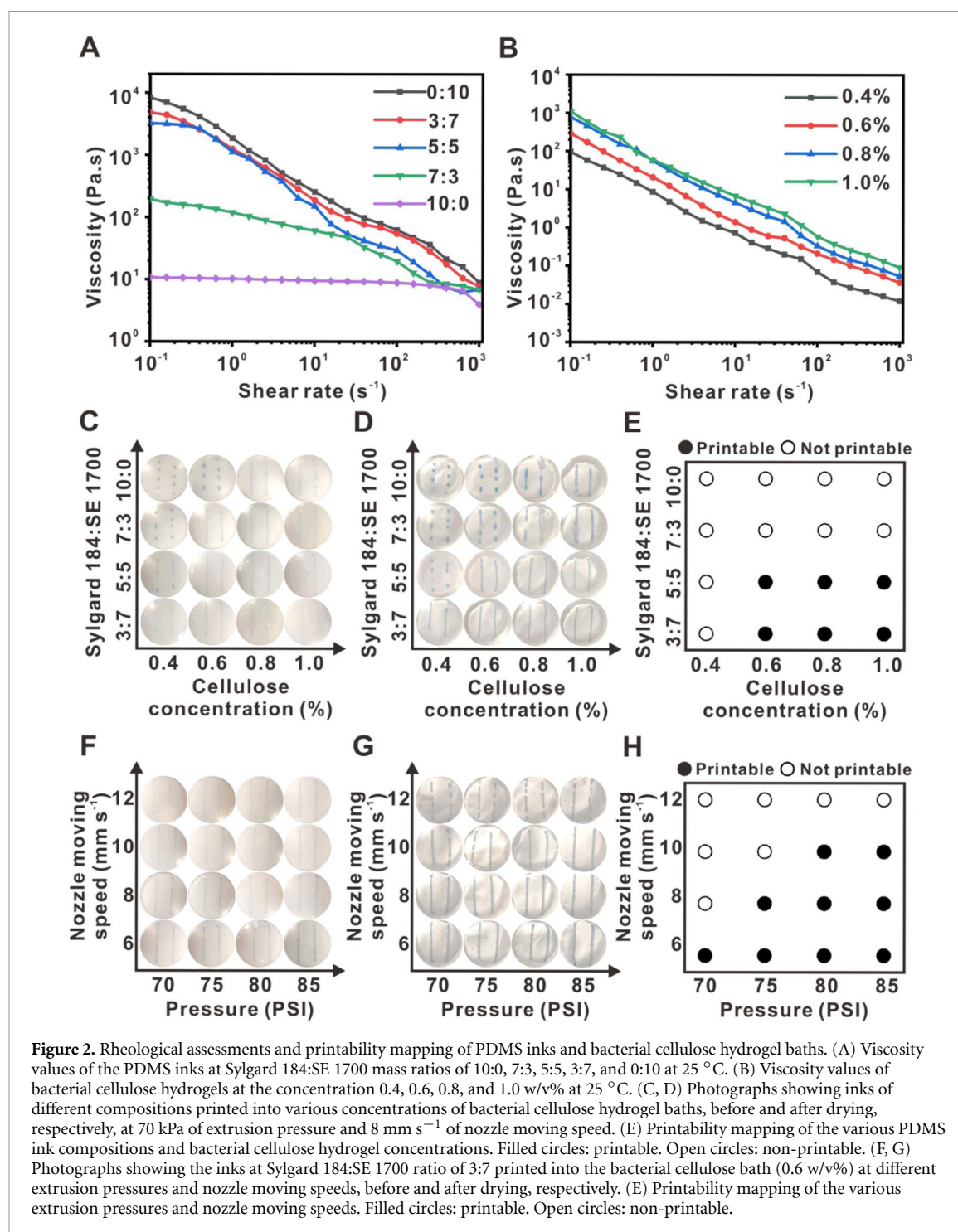
between the ink and the cellulose hydrogel bath, the PDMS ink at the ratio of 3:7 (Sylgard 184:SE 1700) and the 0.6 w/v% of bacterial cellulose suspension were selected for all forthcoming experiments.

We then evaluated the relationship between nozzle moving speed and extrusion pressure *versus* printability. In general, complete microfibrillar structures could be obtained at lower nozzle moving speeds and higher extrusion pressures, whereas the opposite conditions led to formation of imperfect and discontinuous ink microfibers (figures 2(F)–(H)). These results suggested that printing fidelity was enhanced when a larger volume of the PDMS ink was extruded in a specific time frame. Nevertheless, when the nozzle moving speed became too low or the pressure was too high, the printing resolution was reduced causing the extrusion of microfibers significantly thicker than the nozzle diameter. Therefore, we selected 8 mm s^{-1} and 75 psi as the optimized nozzle moving speed and extrusion pressure, respectively, for subsequent printing processes.

Following matrix-assisted printing, the bacterial cellulose hydrogel baths containing embedded PDMS ink patterns were immediately subjected to incubation at 80°C for 2 h, in a confined and humidified container to avoid water evaporation. This process allowed for curing of the PDMS ink filaments into an elastomer maintaining its cylindrical shape. To illustrate that the cured PDMS elastomeric microfibers could be pulled out from the subsequently air-dried paper devices preserving their integrity, we designed and printed several linear patterns featuring a pair of parallel lines (figures S2(A)–(C)) and a sine wavy pattern (figures S2(D)–(G)). We observed that the printed PDMS microfibers were stable and retained their circular cross-sections within the bacterial cellulose matrices both before and after drying/curing. Of note, in both cases the cured PDMS elastomeric microfibers were easily extracted from the paper devices showing well-formed microchannels and there was not any visible color left after the extraction (Videos S1–2). Indeed, due to the hydrophobicity and thermosetting property of PDMS, the printed microfibers were not expected to diffuse into the bacterial cellulose hydrogel baths during the curing process. These different shapes of the microchannels might be suitable for emulating various types of native tissue microarchitectures such as vascular networks and other cannular tissue structures present in the human body.

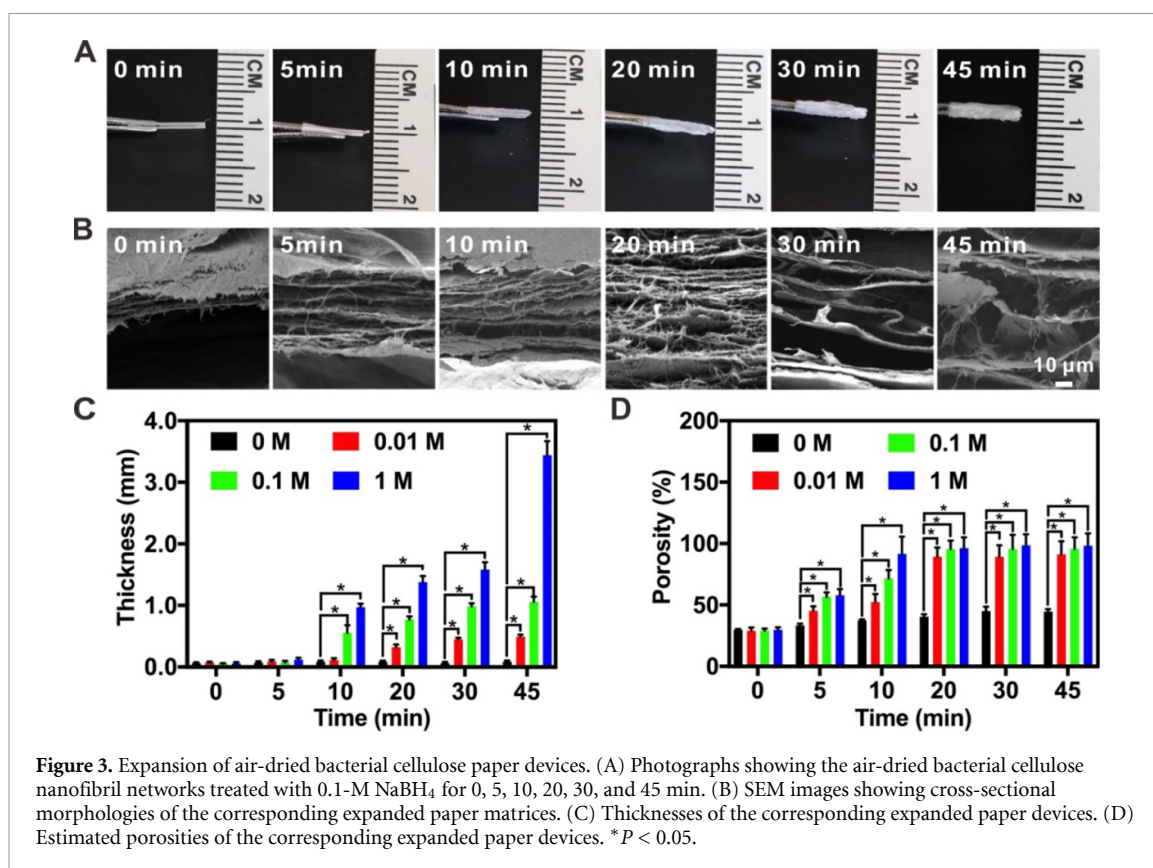
3.3. Expansion of bacterial cellulose paper devices

As we showed in our previous work, a paper device formed by air-drying a bacterial cellulose hydrogel would become extremely dense without assuming a true 3D volume to enable cell penetration [52]. To address this limitation, we adopted a gas-foaming technique [70], to expand these air-dried



paper devices into the third dimension by immersing them in NaBH₄ aqueous solutions (figure 3). As shown in figures 3(A) and (B), layered laminar structures within the paper devices were obtained after vertical expansion [63], where the inter-layer spacing was anticipated to provide appropriate pathways for cell migration and proliferation. The final thickness of the expanded paper devices was increased by prolonging the gas-foaming time in the NaBH₄ solution or elevating the concentration of NaBH₄ (figure 3(C)). Specifically, the thickness of the paper devices grew from an initial 0.72 mm of pre-expansion value to

a total of 3.6 mm after 45 min of treatment with 1-M NaBH₄ solution. Correspondingly, the porosity of the paper devices was also enlarged as the expansion time or the concentration of NaBH₄ was increased (figure 3(D)). While the baseline porosity was merely 33.6%, it was drastically improved to 99.8% after treatment with 1-M NaBH₄ for 45 min. Collectively, our observations supported the fact that the thickness and the porosity of the bacterial cellulose paper devices were positively correlated with the concentration of NaBH₄ and the expansion period, both in a well-controlled manner. Further compression tests



were performed, demonstrating that the compressive moduli of the paper devices treated with 1-M NaBH₄ were worsened by increased expansion time, which corresponds to the multilayer structures formed by gas-foaming (figure S3).

Upon verifying the utility of the gas-foaming method on our air-dried bacterial cellulose matrices, we continued to demonstrate that the same technique was amenable, as well, to expanding the paper devices containing internal microstructures obtained from matrix-assisted printing. The cross-sections of the paper devices possessing a hollow microchannel in the center, after expansion with 0 (water), 0.01, 0.1, and 1 M of NaBH₄ for 5, 10, 20, 30, and 45 min, were photographed (figure 4(A)). The multilayered laminar structures of the expanded, microchannel-embedded paper devices were further characterized using SEM (figure 4(B) and figure S4). Consistent with the results from non-structured paper devices (figure 3), those having embedded PDMS microfibers could also be expanded in their thickness under tight controls by altering the NaBH₄ concentration in the solution and/or the time for expansion. Longer gas-foaming time and higher concentration of NaBH₄ would both result in thicker structures (figure 4(C)) and larger porosities (figure 4(D)). In addition, the diameter of the microchannels embedded in the paper devices slightly increased during the foaming process, such as from 0.73 ± 0.01 to 1.26 ± 0.06 mm when the expansion time was prolonged from 0 to 45 min using the 1-M NaBH₄

aqueous solution (figure 4(E)). This slight expansion of the microchannels in fact, facilitated extraction of the PDMS microfibers post-expansion to obtain intact hollow microchannels.

As expected, the diameter of the bacterial cellulose nanofibrils experienced no significant changes under different expansion conditions (figure 4(F)). By further examining the inner surfaces of the sacrificially printed, microchannel-embedded paper devices using SEM (figure S5), it was clear that the concentration of NaBH₄ and the expansion time also increased the pore size of the expanded bacterial cellulose nanofibril networks, in addition to the inter-layer distances. Importantly, the pore sizes did not exhibit obvious changes even after 45 min of treatment with deionized water (i.e. 0 M of NaBH₄), indicating that swelling itself had a negligible effect on the expansion of the paper matrices. Combining the nanofibrils enabling microstructured surface topography and large surface area-to-volume ratios, the expanded microchannel-embedded paper devices were anticipated to serve as ideal scaffolds to support 3D cell growth.

3.4. Water-absorption of the microchannel-embedded paper devices

The capillary effect, or water-absorption capacity of the expanded paper devices containing embedded microchannels formed by matrix-assisted sacrificial printing, was examined after 5, 10, 20, 30, and

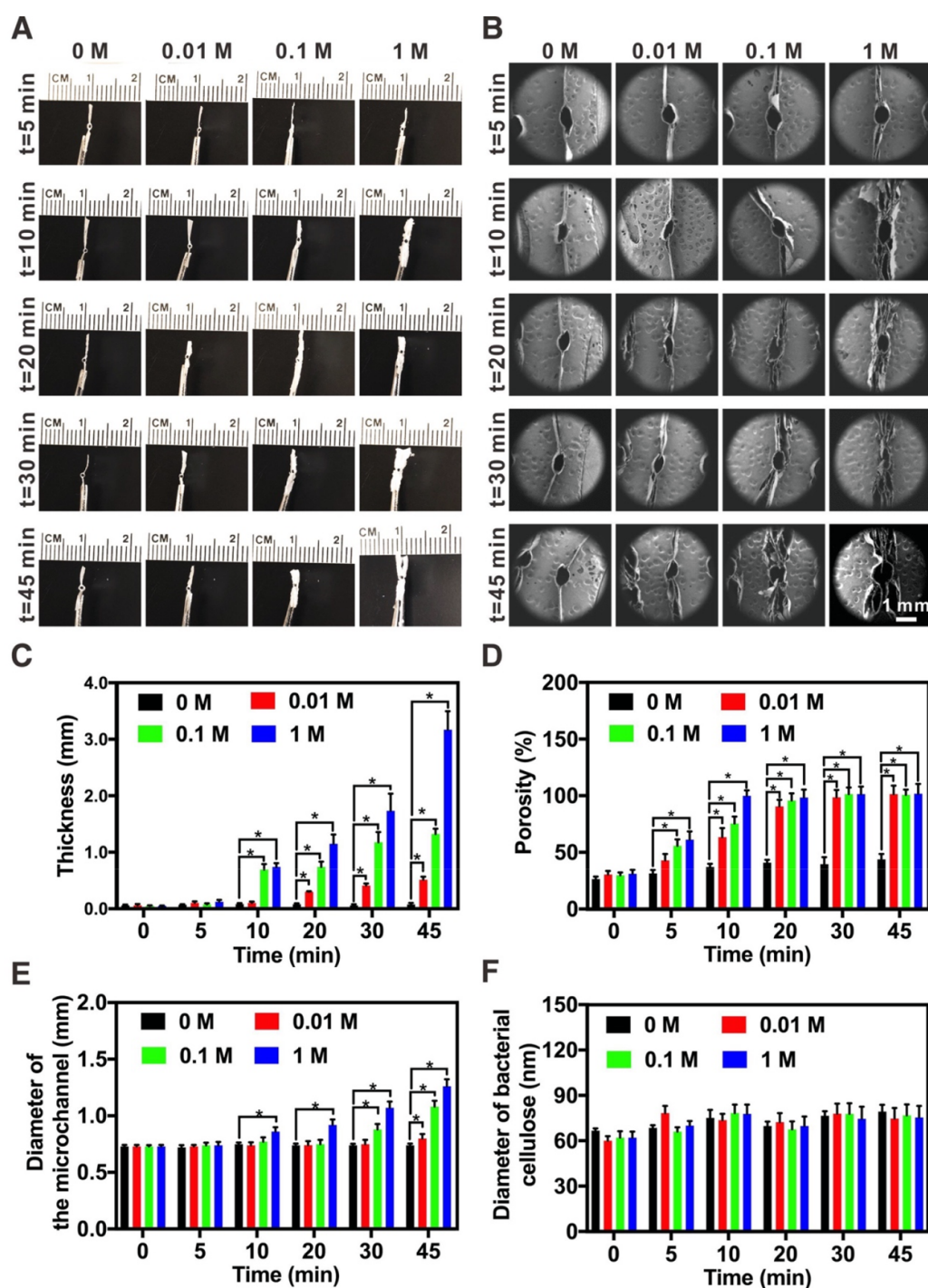


Figure 4. Expansion of the sacrificially printed, microchannel-embedded bacterial cellulose paper devices. (A) Photographs showing the paper devices treated with 0 (deionized water), 0.01, 0.1, and 1 M of NaBH_4 for 5, 10, 20, 30, and 45 min. (B) SEM images showing cross-sectional morphologies of the corresponding expanded paper devices. (C) Thicknesses of the corresponding expanded paper devices. (D) Estimated porosities of the expanded paper devices. (E) Diameters of the microchannels in the corresponding expanded paper devices. (F) Diameters of the bacterial cellulose nanofibrils in the corresponding expanded paper devices. * $P < 0.05$.

45 min of treatment with an aqueous solution of 0.1-M NaBH_4 (figure 5). For each device, a green food dye was first injected into the central microchannel, which could be seen to diffuse into the surrounding bacterial cellulose nanofibril network in a porosity-dependent manner (figure 5(A)). The porosity, as discussed above, was a function of expansion time. As such, with increasing expansion time, the capillary

effect of the paper matrix was more pronounced (figure 5(C)). As an example, by 6 min post-dye injection, >70% of the matrix area was wetted in the paper device expanded for 45 min, while the values were 19.87 ± 1.49 , 37.26 ± 1.14 , 44.21 ± 2.80 , and $48.06 \pm 3.28\%$ in the cases of samples expanded for 5, 10, 20, and 30 min, respectively. These observations indicated that, when endothelial cells are seeded into

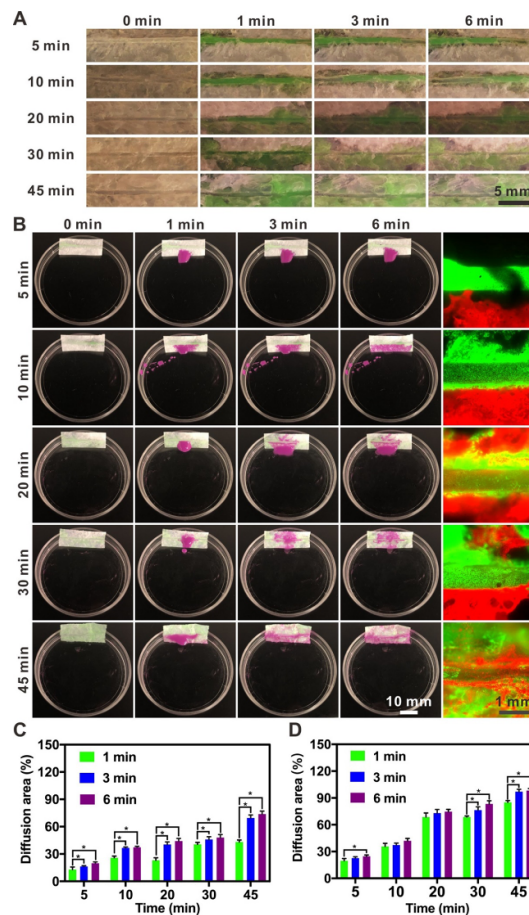


Figure 5. The wicking behaviors of the expanded, microchannel-embedded paper devices. (A), (B) Photographs showing the diffusion of (A) green-colored fluorescent microbeads from the microchannels to the surrounding matrices and (B) red-colored fluorescent microbeads from the peripheries to the bulks of the matrices. (C), (D) The calculated absorption/diffusion areas corresponding to (A) and (B), respectively. * $P < 0.05$.

the microchannels in these paper devices, the higher degree of expansion will likely induce outward diffusion and/or migration of the cells. This phenomenon may lead to the presence of endothelial cells within the surrounding tissue volume, forming a multiscale network otherwise almost impossible without expansion but a dense matrix of entangled bacterial cellulose nanofibrils, as we will demonstrate in the next section.

The transport kinetics of aqueous media was further analyzed from the outside of the microchannels. To this end, we soaked the bottom side of each paper device into a red dye solution and examined the upward dye diffusion/absorption through the capillary force. Indeed, in contrast to the very slow dye transport across the width of the paper matrix expanded for only 5 min (24.7% area coverage by 6 min), the device expanded for 45 min exhibited significantly faster water absorption and diffusion, covering almost the entire area within the same period of 6 min (figures 5(B) and (D)). The improved capillary action would be highly beneficial to allow for inward transport of suspended single cells during the initial seeding process, as well as facilitate subsequent migration and proliferation of cells within

the spaces in between the bacterial cellulose nanofibrils that are otherwise extremely limited without expansion. For our microchannel-embedded bacterial cellulose paper devices, multilayer structures were easily formed by a longer expansion time. However, the longer gas-foaming time could damage the integrity of the microchannels as well as reduce mechanical strengths (figure S3), while the porosity of the paper devices had not been effectively improved. Therefore, the paper devices expanded for 30 min were selected for further experimentation.

3.5. Biological performance of cell-laden constructs

A scaffold plays an important role to generate a biomimetic tissue model, providing not only the microarchitecture shaping the internal and overall structures of the tissue but also a substrate supporting cellular adhesion and functions. In previous studies, the fugitive ink Pluronic F127 and gelatin were used to fabricate customized hydrogel-based tissue constructs with the embedded vascular microchannels [71–73]. While they allow embedment of living cells during fabrication, they suffer from short shelf-lives requiring their immediate usage post-fabrication,

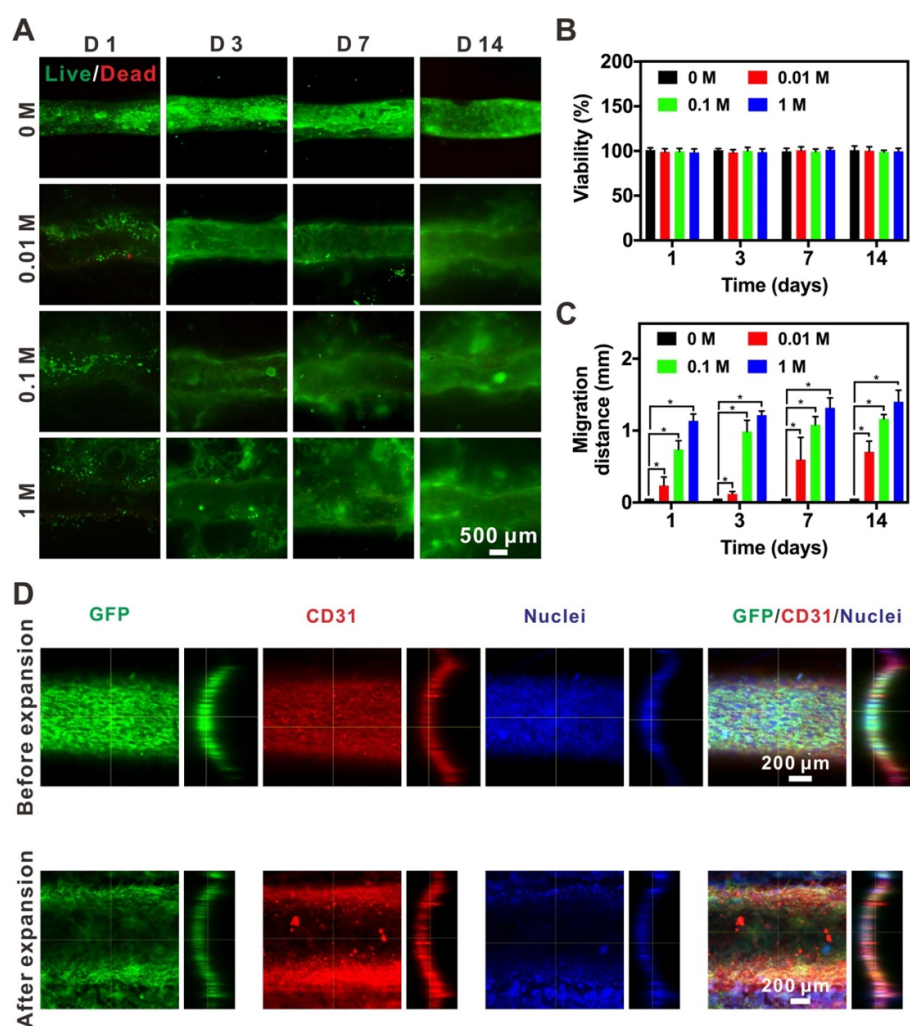


Figure 6. Endothelialization of the microchannels of the paper devices before and after expansion in NaBH_4 for 30 min. (A) Fluorescence micrographs showing Live/Dead staining at 1, 3, 7, and 14 d of culture, respectively. (B) Quantitative analysis of cell viability. (C) The diffusion/migration distance of HUVECs from the microchannels into the surrounding bacterial cellulose matrices. (D) Confocal projection views of the microchannel region populated with GFP-HUVECs in the paper device before and after expansion into 0.1-M NaBH_4 solution for 30 min, which were also stained for CD31 (red) and nuclei (blue), at 14 d of culture. * $P < 0.05$.

thus limiting their on-demand production and utilization in particular when *in vitro* tissue modeling is the primary purpose. To address such an issue, microchannel-embedded paper devices fabricated via matrix-embedded sacrificial printing are good candidates for constructing vascularized tissue models since they feature essentially unlimited shelf-lives in the dry state. In our previous demonstration, we generated a vascularized breast tumor model by seeding HUVECs into the hollow microchannels followed by culturing MCF-7 breast tumor cells in the surrounding paper matrices [52]. Nevertheless, neither the HUVECs could migrate out into the bacterial cellulose networks from the interior surfaces of the microchannels, nor the MCF-7 cells grown on the exterior surfaces of the paper devices were able to penetrate into the matrices. Consequently, the formed vascularized breast tumor model was largely pseudo-3D in nature containing cells only on the surfaces of the different compartments.

To understand if the expanded paper devices would facilitate the formation of multiscale vascular networks, HUVECs were seeded into the microchannels of the paper devices subjected to varying degrees of expansion, i.e. those expanded in 0, 0.01, 0.1, or 1 M of NaBH_4 for 30 min (figure 6). Fluorescence micrographs were taken at 1, 3, 7, and 14 d post-seeding, showing that the cells were homogeneously distributed on the interior surfaces of the microchannels and proliferated during the culture period (figure 6(A)). Viability analyses revealed that the percentages of viable cells in all cases approached 100%, suggesting good biocompatibility of the devices both before and after expansion (figures 6(A) and (B)). Interestingly, the diffusion/migration distance of the HUVECs from the microchannel to the surrounding matrix was positively correlated with the level of expansion of the bacterial cellulose network, where improved cell infiltration was observed as the paper device became increasingly porous (figure 6(C)). This

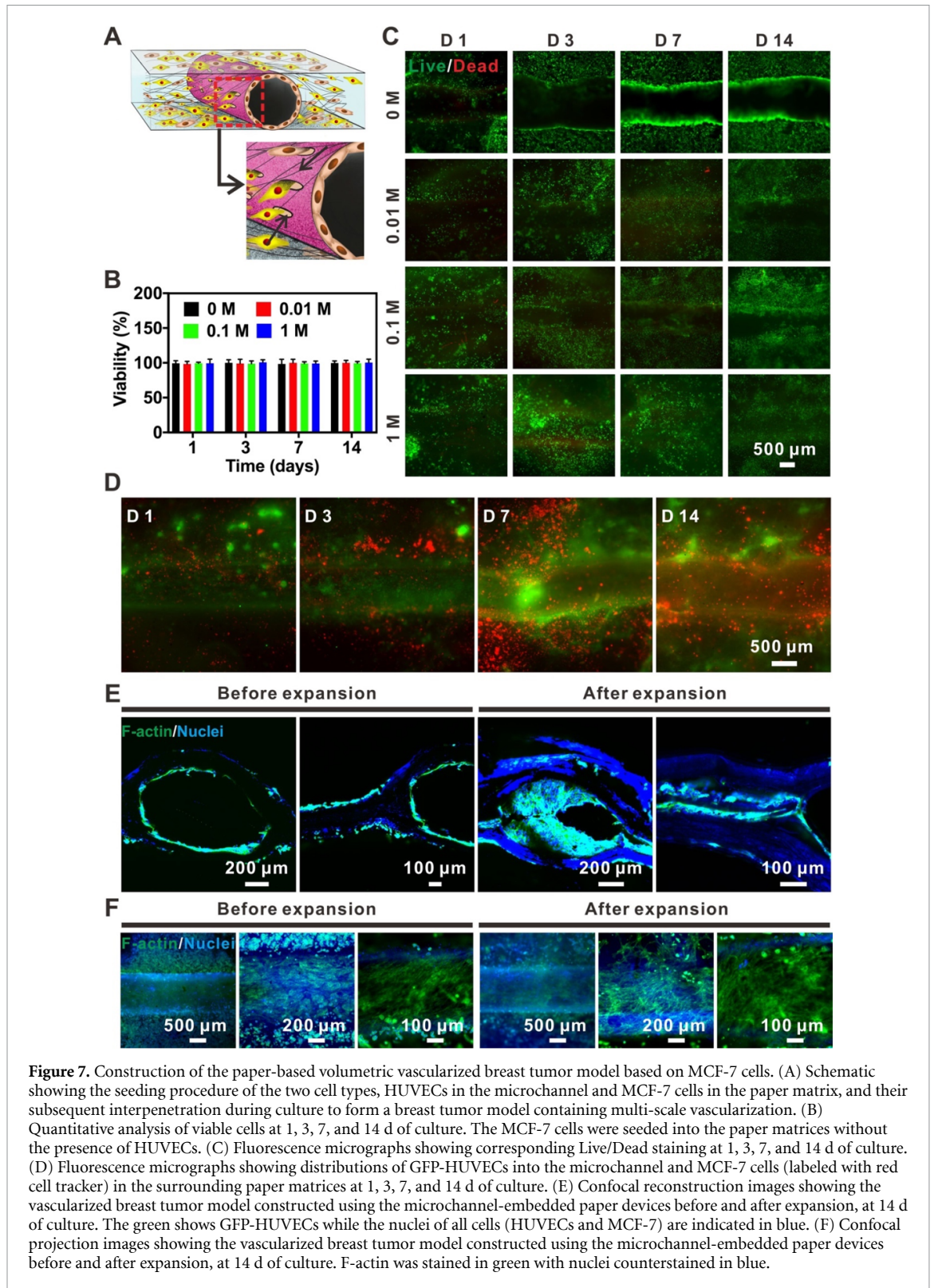
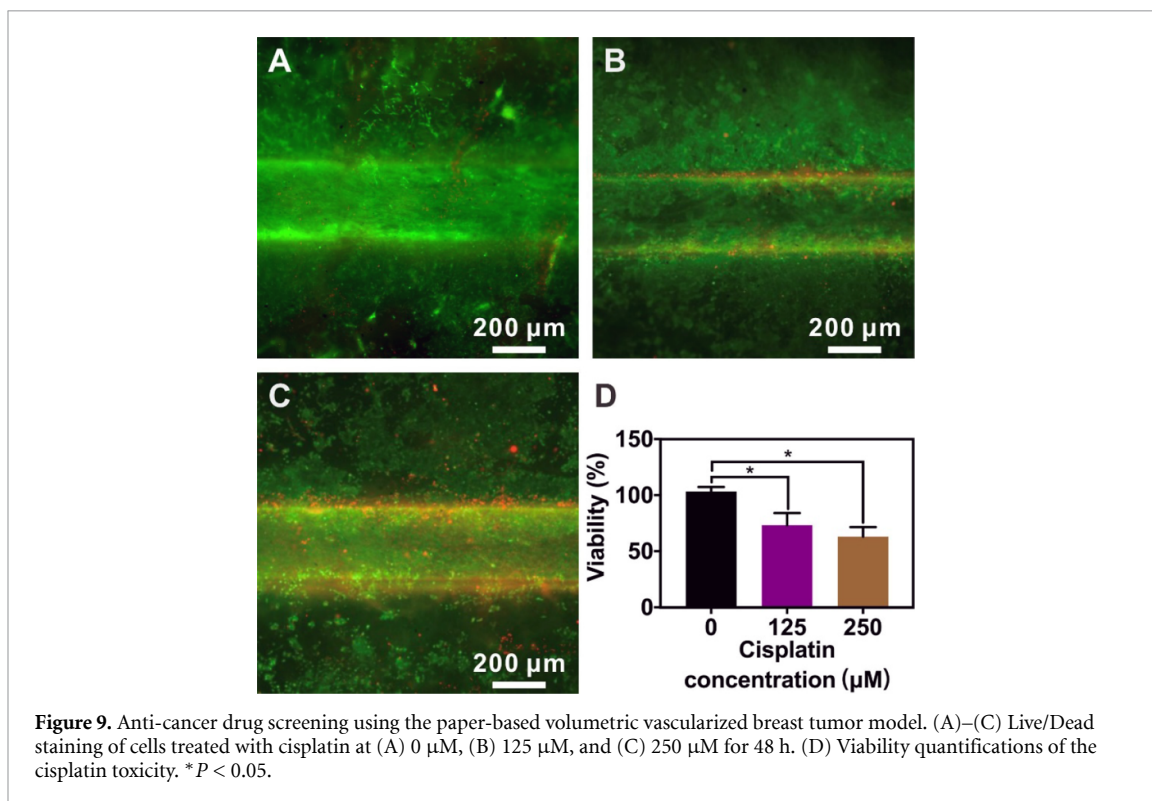
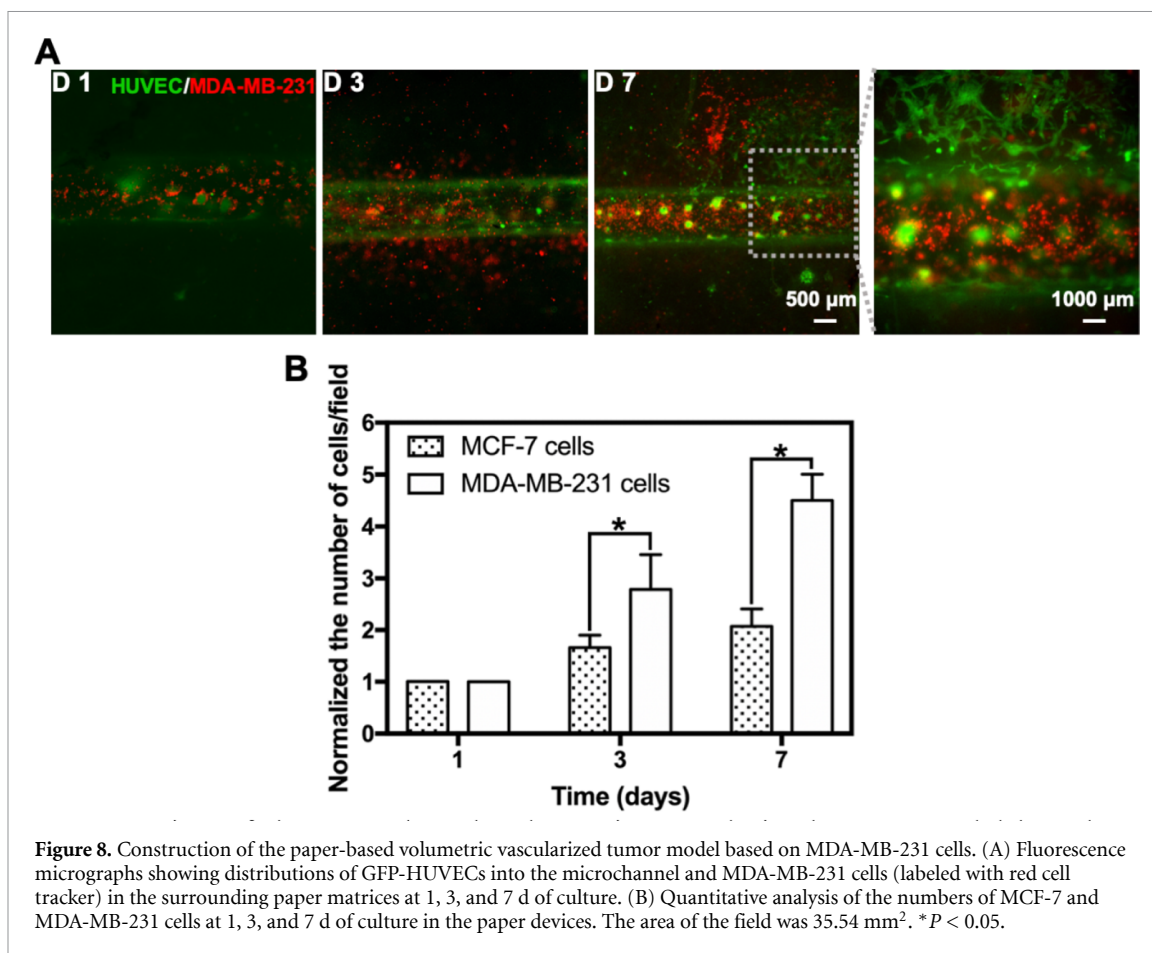


Figure 7. Construction of the paper-based volumetric vascularized breast tumor model based on MCF-7 cells. (A) Schematic showing the seeding procedure of the two cell types, HUVECs in the microchannel and MCF-7 cells in the paper matrix, and their subsequent interpenetration during culture to form a breast tumor model containing multi-scale vascularization. (B) Quantitative analysis of viable cells at 1, 3, 7, and 14 d of culture. The MCF-7 cells were seeded into the paper matrices without the presence of HUVECs. (C) Fluorescence micrographs showing corresponding Live/Dead staining at 1, 3, 7, and 14 d of culture. (D) Fluorescence micrographs showing distributions of GFP-HUVECs into the microchannel and MCF-7 cells (labeled with red cell tracker) in the surrounding paper matrices at 1, 3, 7, and 14 d of culture. (E) Confocal reconstruction images showing the vascularized breast tumor model constructed using the microchannel-embedded paper devices before and after expansion, at 14 d of culture. The green shows GFP-HUVECs while the nuclei of all cells (HUVECs and MCF-7) are indicated in blue. (F) Confocal projection images showing the vascularized breast tumor model constructed using the microchannel-embedded paper devices before and after expansion, at 14 d of culture. F-actin was stained in green with nuclei counterstained in blue.

result was consistent with SEM characterizations of the bulk pore sizes in the layered laminar structures and the inter-nanofibril pore sizes on the surfaces of the microchannels, as well as the dye transport assessments, in relation with expansion of the devices using the NaBH_4 solutions (figures 3–5 and figures S4–5). The unexpanded, as-prepared paper devices exhibited no visible outward penetration of cells from the

microchannel, which agreed well with our previous report [52].

In addition, endothelial-specific biomarker expression by HUVECs forming the intact endothelial barriers on the inner surfaces of the microchannels was studied by immunostaining. Similar to the non-expanded microchannel, the endothelium formed on the microchannel in the expanded



paper device also indicated the monolayer nature and good expression of CD31, revealing the possible functionality (figure 6(D)). As shown in figure S6, the microchannel region populated with HUVECs in the paper devices after expansion, revealed satisfactorily homogeneous distribution of HUVECs along the microchannel.

Furthermore, the MCF-7 breast tumor cells were seeded into the bacterial cellulose matrices treated with 0, 0.01, 0.1, or 1 M of NaBH_4 for 30 min, and then cultured for up to 14 d (figure 7(A)). While viability analyses suggested very high viable counts of these cells (figure 7(B)), fluorescence images revealed that the cells were uniformly distributed across the entire area of each device during the culture period (figure 7(C)). According to these results, we chose the dosage/time of 0.1-M NaBH_4 for expansion of our paper devices for 30 min as a typical condition for the fabrication of our vascularized tumor model. Nevertheless, the optimal parameters for the expansion of the paper devices will eventually depend on the intended specific applications.

Then, we explored the feasibility of generating a vascularized breast tumor model by combining the two cell types together (figure 7(A)). We seeded HUVECs into the microchannels of the expanded paper devices, and MCF-7 cells into the surrounding bacterial cellulose matrices. From figure 7(D), it could be derived that the HUVECs and MCF-7 cells were able to obtain a highly interpenetrating configuration in the co-culture, forming a breast tumor model embedded with a multiscale vascular network. This result demonstrated that the migration degree of the MCF-7 cells from the surface of the paper device to the underlying matrix and the microchannel was positively correlated with expansion of the bacterial cellulose network, where improved MCF-7 cell infiltration was observed as the paper device became increasingly porous. This configuration was also validated in confocal observations of the cross-sections, comparing those from a non-expanded paper device and the expanded paper device (figure 7(E)). Consistent with the observation in our previous report [52], without expansion the respective cell types were entirely confined to their original compartments, i.e. HUVECs in the microchannels and MCF-7 on the exterior surfaces. In the expanded paper device, in comparison, a 3D tissue model could be well-formed with not only out-sprouting endothelial cells but also inward infiltrating breast tumor cells. F-actin staining of both cell types at 14 d of culture further proved their good spreading (figure 7(F)).

Knowing that MCF-7 cells are less invasive breast tumor cells, a more invasive cell type, MDA-MB-231 cells, was further used to better mimic the biological situation of metastatic tumors. Indeed, the highly interpenetrating configuration of the HUVECs and the MDA-MB-231 cells was observed (figure 8(A)).

In addition, the proliferation rate of the MDA-MB-231 cells was higher than that of the MCF-7 cells in the models (figure 8(B)), which might be attributed to the stronger invasive ability of the former. These results suggested that our gas-foaming strategy could offer a favorable microenvironment facilitating cell interactions in a volumetric manner and construction of improved paper-based tissue models in 3D.

3.6. Drug treatment

Breast cancer is one of the leading causes of mortality in the female population worldwide [74]. Being able to create biomimetic *in vitro* models for accurate screening of anti-cancer agents during the drug development process and for precise selection of anti-cancer therapeutics to individual patients, is in strong demand [20, 75]. To this end, we intended to finally demonstrate a proof-of-concept utility of our volumetric vascularized breast tumor model in screening anti-cancer drugs. Cisplatin is an important chemotherapeutic agent widely used for the treatment of a variety of malignancies, including breast cancers [76]. To examine the responses of our expanded paper device-based breast tumor model, 0, 125, or 250 μM of cisplatin was injected from the endothelialized microchannels and incubated for another 48 h. As revealed by figure 9, cisplatin exerted a dose-dependent toxicity profile, suggesting the potential of these volumetric tissue models in intended application areas.

4. Conclusions

In summary, we have demonstrated a simple yet highly controllable gas-foaming method for expanding sacrificially printed paper devices containing embedded microchannels, for the construction of volumetric tissue models. This study represents a comprehensive analysis of printability of the fugitive PDMS inks within the bacterial cellulose hydrogel baths, while water evaporation through air-drying of the bacterial cellulose hydrogel and removal of the PDMS microfibers after curing led to formation of perfusable microchannels in paper devices. Upon subsequent expansion, the paper matrices became highly porous featuring layered structures, while simultaneously retaining the intact entangled bacterial cellulose nanofibril networks. More interestingly, the expanded microchannel-embedded paper devices supported cellular infiltration and proliferation throughout bulk of the resultant tissues, potentially providing a new way to engineer vascularized tissue models or alike toward applications in preclinical drug screening and personalized therapeutic selection. Finally, it should be emphasized that the new method reported in this paper does not necessarily increase the cost associated with these

microchannel-embedded paper-based devices comparing to our previous strategy [52]. As indicated in figure S7 and Table S1, the material cost for each device was calculated to be still under 4 cents.

Acknowledgments

The authors gratefully acknowledge funding from the National Institutes of Health (K99CA201603, R00CA201603, R21EB025270, R21EB026175, R01EB028143), the Brigham Research Institute, and the New England Anti-Vivisection Society. G. Trujillo-de Santiago and M.M. Alvarez gratefully acknowledge funding from CONACyT and the Tecnológico de Monterrey-MIT Nanotechnology Program.

Conflicts of interest

There is no conflict of interest to declare.

Data Availability

The raw data required to reproduce these findings are available upon request.

ORCID iD

Yu Shrike Zhang  <https://orcid.org/0000-0002-0045-0808>

References

- Papaioannou T G, Manolesou D, Dimakakos E, Tsoucalas G, Vavuranakis M and Tousoulis D 2019 3D bioprinting methods and techniques: Applications on artificial blood vessel fabrication *Acta Cardiol. Sin.* **35** 284–9
- Mandrycky C, Wang Z, Kim K and Kim D-H 2016 3D bioprinting for engineering complex tissues *Biotechnol. Adv.* **34** 422–34
- McCracken J M, Rauzan B M, Kjellman J C E, Kandel M E, Liu Y H, Badea A, Miller L A, Rogers S A, Popescu G and Nuzzo R G 2019 3D-printed hydrogel composites for predictive temporal (4D) cellular organizations and patterned biogenic mineralization *Adv. Healthcare Mater.* **8** e1800788
- Farina M et al 2017 3D printed vascularized device for subcutaneous transplantation of human islets *Biotechnol. J.* **12** 1700169
- Kim B S, Jang J, Chae S, Gao G, Kong J S, Ahn M and Cho D W 2016 Three-dimensional bioprinting of cell-laden constructs with polycaprolactone protective layers for using various thermoplastic polymers *Biofabrication* **8** 035013
- Won J Y, Park C Y, Bae J H, Ahn G, Kim C, Lim D H, Cho D W, Yun W S, Shim J H and Huh J B 2016 Evaluation of 3D printed PCL/PLGA/ β -TCP versus collagen membranes for guided bone regeneration in a beagle implant model *Biomed. Mater.* **11** 055013
- Yang Y et al 2019 Elastic 3D-printed hybrid polymeric scaffold improves cardiac remodeling after myocardial infarction *Adv. Healthcare Mater.* **8** e1900065
- McBeth C, Lauer J, Ottersbach M, Campbell J, Sharon A and Sauer-Budge A F 2017 3D bioprinting of GelMA scaffolds triggers mineral deposition by primary human osteoblasts *Biofabrication* **9** 015009
- Xie M et al 2019 Electro-assisted bioprinting of low-concentration GelMA microdroplets *Small* **15** e1804216
- Hong S, Sycks D, Chan H F, Lin S, Lopez G P, Guilak F, Leong K W and Zhao X 2015 3D printing: 3D printing of highly stretchable and tough hydrogels into complex, cellularized structures *Adv. Mater.* **27** 4035–40
- Wang X Y, Jin Z H, Gan B W, Lv S W, Xie M and Huang W H 2014 Engineering interconnected 3D vascular networks in hydrogels using molded sodium alginate lattice as the sacrificial template *Lab Chip* **14** 2709–16
- Garcia-Lizarribar A, Fernandez-Garibay X, Velasco-Mallorqui F, Castano A G, Samitier J and Ramon-Azcon J 2018 Composite biomaterials as long-lasting scaffolds for 3D bioprinting of highly aligned muscle tissue *Macromol. Biosci.* **18** e1800167
- Liu W, Zhong Z, Hu N, Zhou Y, Maggio L, Miri A K, Fragasso A, Jin X, Khademhosseini A and Zhang Y S 2018 Coaxial extrusion bioprinting of 3D microfibrous constructs with cell-favorable gelatin methacryloyl microenvironments *Biofabrication* **10** 024102
- Tao J et al 2019 Rapid 3D printing of functional nanoparticle-enhanced conduits for effective nerve repair *Acta Biomater.* **90** 49–59
- Do A V, Akkouch A, Green B, Ozbolat I, Debabneh A, Geary S and Salem A K 2017 Controlled and sequential delivery of fluorophores from 3D printed alginate-PLGA tubes *Ann. Biomed. Eng.* **45** 297–305
- Arslan-Yildiz A, El Assal R, Chen P, Guven S, Inci F and Demirci U 2016 Towards artificial tissue models: past, present, and future of 3D bioprinting *Biofabrication* **8** 014103
- Xu C, Dai G and Hong Y 2019 Recent advances in high-strength and elastic hydrogels for 3D printing in biomedical applications *Acta Biomater.* **95** 50–9
- Lee S, Ko J, Park D, Lee S R, Chung M, Lee Y and Jeon N L 2018 Microfluidic-based vascularized microphysiological systems *Lab Chip* **18** 2686–709
- Fedorovich N E, Swennen I, Girones J, Moroni L, van Blitterswijk C A, Schacht E, Alblas J and Dhert W J 2009 Evaluation of photocrosslinked Lutrol hydrogel for tissue printing applications *Biomacromolecules* **10** 1689–96
- Esch E W, Bahinski A and Huh D 2015 Organs-on-chips at the frontiers of drug discovery *Nat. Rev. Drug Discovery* **14** 248–60
- Cheng S Y, Heilman S, Wasserman M, Archer S, Shuler M L and Wu M 2007 A hydrogel-based microfluidic device for the studies of directed cell migration *Lab Chip* **7** 763–9
- Sharifi F et al 2019 A foreign body response-on-a-chip platform *Adv. Healthcare Mater.* **8** e1801425
- Tan T, Hu H, Wang H, Li J, Wang Z, Wang J, Wang S, Zhang Z and Li Y 2019 Bioinspired lipoproteins-mediated photothermia remodels tumor stroma to improve cancer cell accessibility of second nanoparticles *Nat. Commun.* **10** 3322
- Patolsky F, Zheng G and Lieber C M 2006 Fabrication of silicon nanowire devices for ultrasensitive, label-free, real-time detection of biological and chemical species *Nat. Protoc.* **1** 1711–24
- Bhatia S N and Ingber D E 2014 Microfluidic organs-on-chips *Nat. Biotechnol.* **32** 760–72
- Yesil-Celiktas O, Hassan S, Miri A K, Maharjan S, Al-kharboosh R, Quinones-Hinojosa A and Zhang Y S 2018 Mimicking human pathophysiology in organ-on-chip devices *Adv. Biosyst.* **2** 1800109
- Zhang Y S et al 2017 Multisensor-integrated organs-on-chips platform for automated and continual in situ monitoring of organoid behaviors *Proc. Natl Acad. Sci. USA* **114** E2293–E302
- Avery R K, Albadawi H, Akbari M, Zhang Y S, Duggan M J, Sahani D V, Olsen B D, Khademhosseini A and Oklu R 2016 An injectable shear-thinning biomaterial for endovascular embolization *Sci. Trans. Med.* **8** 365ra156
- Dauth S, Maoz B M, Sheehy S P, Hemphill M A, Murty T, Macedonia M K, Greer A M, Budnik B and Parker K K 2017

- Neurons derived from different brain regions are inherently different in vitro: a novel multiregional brain-on-a-chip *J. Neurophysiol.* **117** 1320–41
- [30] Takeda S *et al* 2015 Neuronal uptake and propagation of a rare phosphorylated high-molecular-weight tau derived from Alzheimer's disease brain *Nat. Commun.* **6** 8490
- [31] Zhang Y S *et al* 2016 Bioprinting 3D microfibrinous scaffolds for engineering endothelialized myocardium and heart-on-a-chip *Biomaterials* **110** 45–59
- [32] Huh D, Matthews B D, Mammoto A, Montoya-Zavala M, Hsin H Y and Ingber D E 2010 Reconstituting organ-level lung functions on a chip *Science* **328** 1662–8
- [33] Seo J, Byun W Y, Alisafaei F, Georgescu A, Yi Y S, Massaro-Giordano M, Shenoy V B, Lee V, Bunya V Y and Huh D 2019 Multiscale reverse engineering of the human ocular surface *Nat. Med.* **25** 1310–8
- [34] de Haan P, Ianovska M A, Mathwig K, van Lieshout G A A, Triantis V, Bouwmeester H and Verpoorte E 2019 Digestion-on-a-chip: a continuous-flow modular microsystem recreating enzymatic digestion in the gastrointestinal tract *Lab Chip* **19** 1599–609
- [35] Powers M J *et al* 2002 A microfabricated array bioreactor for perfused 3D liver culture *Biotechnol. Bioeng.* **78** 257–69
- [36] Jang K J and Suh K Y 2010 A multi-layer microfluidic device for efficient culture and analysis of renal tubular cells *Lab Chip* **10** 36–42
- [37] Agrawal G, Aung A and Varghese S 2017 Skeletal muscle-on-a-chip: an in vitro model to evaluate tissue formation and injury *Lab Chip* **17** 3447–61
- [38] Marturano-Kruik A, Nava M M, Yeager K, Chramiec A, Hao L, Robinson S, Guo E, Raimondi M T and Vunjak-Novakovic G 2018 Human bone perivascular niche-on-a-chip for studying metastatic colonization *Proc. Natl Acad. Sci. USA* **115** 1256–61
- [39] Gottardi R 2019 Load-induced osteoarthritis on a chip *Nat. Biomed. Eng.* **3** 502–3
- [40] Papapetrou E P 2016 Patient-derived induced pluripotent stem cells in cancer research and precision oncology *Nat. Med.* **22** 1392–401
- [41] Osaki T, Shin Y, Sivathanu V, Campisi M and Kamm R D 2018 In vitro microfluidic models for neurodegenerative disorders *Adv. Healthcare Mater.* **7** 1700489
- [42] Wang J, Zhao L, Zhang A, Huang Y, Tavakoli J and Tang Y 2018 Novel bacterial cellulose/gelatin hydrogels as 3D scaffolds for tumor cell culture *Polymers* **10** 581
- [43] Gao M, Li J, Bao Z, Hu M, Nian R, Feng D, An D, Li X, Xian M and Zhang H 2019 A natural in situ fabrication method of functional bacterial cellulose using a microorganism *Nat. Commun.* **10** 437
- [44] Kirdponpattara S, Phisalaphong M and Kongruang S 2017 Gelatin-bacterial cellulose composite sponges thermally cross-linked with glucose for tissue engineering applications *Carbohydr. Polym.* **177** 361–8
- [45] Pahlevan M, Toivakka M and Alam P 2018 Mechanical properties of TEMPO-oxidised bacterial cellulose-amino acid biomaterials *Eur. Polym. J.* **101** 29–36
- [46] Backdahl H, Helenius G, Bodin A, Nannmark U, Johansson B R, Risberg B and Gatenholm P 2006 Mechanical properties of bacterial cellulose and interactions with smooth muscle cells *Biomaterials* **27** 2141–9
- [47] Mangayil R K, Rajala S M, Pammo A J, Sarlin E L, Luo J, Santala V P, Karp M T and Tuukkanen S R 2017 Engineering and characterization of bacterial nanocellulose films as low cost and flexible sensor material *ACS Appl. Mater. Interfaces* **9** 19048–56
- [48] Gatenholm P and Klemm D 2011 Bacterial nanocellulose as a renewable material for biomedical applications *MRS Bull* **35** 208–13
- [49] Favi P M, Benson R S, Neilsen N R, Hammonds R L, Bates C C, Stephens C P and Dhar M S 2013 Cell proliferation, viability, and in vitro differentiation of equine mesenchymal stem cells seeded on bacterial cellulose hydrogel scaffolds *Mater. Sci. Eng. C* **33** 1935–44
- [50] Zaborowska M, Bodin A, Backdahl H, Popp J, Goldstein A and Gatenholm P 2010 Microporous bacterial cellulose as a potential scaffold for bone regeneration *Acta Biomater.* **6** 2540–7
- [51] Cai Z and Kim J 2010 Preparation and characterization of novel bacterial cellulose/gelatin scaffold for tissue regeneration using bacterial cellulose hydrogel *J. Nanotechnol. Eng. Med.* **1** 021002
- [52] Cheng F *et al* 2019 Generation of cost-effective paper-based tissue models through matrix-assisted sacrificial 3d printing *Nano Lett.* **19** 3603–11
- [53] Ainla A, Hamed M M, Güder F and Whitesides G M 2017 Electrical textile valves for paper microfluidics *Adv. Mater.* **29** 1702894
- [54] Hamed M M, Ainla A, Guder F, Christodouleas D C, Fernandez-Abedul M T and Whitesides G M 2016 Integrating electronics and microfluidics on paper *Adv. Mater. Weinheim* **28** 5054–63
- [55] Hagyu H, Ifuku S and Nogi M 2017 Acetylation of optically transparent cellulose nanopaper for high thermal and moisture resistance in a flexible device substrate *Flex. Print. Electron.* **2** 014003
- [56] Jiang J, Carlson M A, Teusink M J, Wang H, MacEwan M R and Xie J 2015 Expanding two-dimensional electrospun nanofiber membranes in the third dimension by a modified gas-foaming technique *ACS Biomater. Sci. Eng.* **1** 991–1001
- [57] Li W J and Tuan R S 2009 Fabrication and application of nanofibrous scaffolds in tissue engineering *Curr. Protocols Cell Biol.* **Chapter 25** Unit 25 22
- [58] Chen S, Li R, Li X and Xie J 2018 Electrospinning: An enabling nanotechnology platform for drug delivery and regenerative medicine *Adv. Drug. Deliv. Rev.* **132** 188–213
- [59] Hu Y, Catchmark J M, Zhu Y, Abidi N, Zhou X, Wang J and Liang N 2014 Engineering of porous bacterial cellulose toward human fibroblasts ingrowth for tissue engineering *J. Mater. Res.* **29** 2682–93
- [60] Svensson A, Nicklasson E, Harrah T, Panilaitis B, Kaplan D L, Brittberg M and Gatenholm P 2005 Bacterial cellulose as a potential scaffold for tissue engineering of cartilage *Biomaterials* **26** 419–31
- [61] Xiong G, Luo H, Zhu Y, Raman S and Wan Y 2014 Creation of macropores in three-dimensional bacterial cellulose scaffold for potential cancer cell culture *Carbohydr. Polym.* **114** 553–7
- [62] Xiong G, Luo H, Gu F, Zhang J, Hu D and Wan Y 2013 A novel in vitro three-dimensional macroporous scaffolds from bacterial cellulose for culture of breast cancer cells *J. Biomater. Nanobiotechnol.* **04** 316–26
- [63] Jiang J, Li Z, Wang H, Wang Y, Carlson M A, Teusink M J, MacEwan M R, Gu L and Xie J 2016 Expanded 3D nanofiber scaffolds: Cell penetration, neovascularization, and host response *Adv. Healthcare Mater.* **5** 2993–3003
- [64] Chen S, Carlson M A, Zhang Y S, Hu Y and Xie J 2018 Fabrication of injectable and superelastic nanofiber rectangle matrices ("peanuts") and their potential applications in hemostasis *Biomaterials* **179** 46–59
- [65] Nakayama A, Kakugo A, Gong J P, Osada Y, Takai M, Erata T and Kawano S 2004 Synthesis of cellulose-based double-network hydrogels demonstrating high strength, self-healing, and antibacterial properties *Adv. Funct. Mater.* **14** 1124–8
- [66] Ozbolat V, Dey M, Ayan B, Povilianskas A, Demirel M C and Ozbolat I T 2018 3D printing of PDMS improves its mechanical and cell adhesion properties *ACS Biomater. Sci. Eng.* **4** 682–93
- [67] Yadav M and Xu Q 2012 Liquid-phase chemical hydrogen storage materials *Energy Environ. Sci.* **5** 9698–725
- [68] Mohite B V, Koli S H and Patil S V 2019 Bacterial cellulose-based hydrogels: synthesis, properties, and applications *Cellulose-Based Superabsorbent Hydrogels* Mondal Md. I. H. (Berlin: Springer) pp 1255–76
- [69] Dutta S D, Patel D K and Lim K T 2019 Functional cellulose-based hydrogels as extracellular matrices for tissue engineering *J. Biol. Eng.* **13** 55

- [70] Chen S, Wang H, McCarthy A, Yan Z, Kim H J, Carlson M A, Xia Y and Xie J 2019 Three-dimensional objects consisting of hierarchically assembled nanofibers with controlled alignments for regenerative medicine *Nano Lett.* **19** 2059–65
- [71] Kolesky D B, Truby R L, Gladman A S, Busbee T A, Homan K A and Lewis J A 2014 3D bioprinting of vascularized, heterogeneous cell-laden tissue constructs *Adv. Mater.* **26** 3124–30
- [72] Ouyang L, Armstrong J P K, Chen Q, Lin Y and Stevens M M 2019 Void-free 3d bioprinting for in situ endothelialization and microfluidic perfusion *Adv. Funct. Mater.* **30** 1908349
- [73] Kolesky D B, Homan K A, Skylar-Scott M A and Lewis J A 2016 Three-dimensional bioprinting of thick vascularized tissues *Proc. Natl Acad. Sci.* **113** 3179–84
- [74] Torre L A, Islami F, Siegel R L, Ward E M and Jemal A 2017 Global cancer in women: Burden and trends *Cancer Epidemiol. Biomarkers Prev.* **26** 444–57
- [75] Zhang Y S 2019 The ultimate in personalized medicine: your body on a chip *IEEE Spectrum* (Piscataway, NJ: IEEE)
- [76] Dasari S and Tchounwou P B 2014 Cisplatin in cancer therapy: Molecular mechanisms of action *Eur. J. Pharmacol.* **740** 364–78